Control of nanoscale precipitation and elimination of intermediatetemperature embrittlement in multicomponent high-entropy alloys

T. Yang[a,b], Y.L. Zhao[b,c], L. Fan[d], J. Wei[b,e], J.H. Luan[b], W.H. Liu[b,f], C. Wang[a], Z.B. Jiao[d], J.J. Kai[a,b,c], C.T. Liu[a,b,*]

[a] Department of Materials Science and Engineering, City University of Hong Kong, Hong Kong, China

[b] Department of Mechanical Engineering, City University of Hong Kong, Hong Kong, China

[c] Center for Advanced Nuclear Safety and Sustainable Development, City University of Hong Kong, Hong Kong, China

[d] Department of Mechanical Engineering, The Hong Kong Polytechnic University, Hong Kong, China

[e] School of Physics and Electronic Engineering, Linyi University, Linyi, China

[f] School of Materials Science and Engineering, Harbin Institute of Technology, Shenzhen, PR China

Abstract

Thermally stable high-entropy alloys (HEAs) consisting of a high density of coherent precipitates show a great potential for high-temperature applications. In this work, we systematically investigated the phase sta- bility and coarsening kinetics of $L1_2$-type coherent precipitates in a Ni-30Co-13Fe-15Cr-6Al-6Ti-0.1B (at.%) HEA isothermally aged at 800, 900 and 1000°C. Aged microstructures in the grain interiors under this temperature range were essentially dominated by the uniform precipitation of multicomponent $L1_2$ (Ni, Co, Fe, Cr)$_3$(Ti, Al)-type precipitates. The coarsening kinetics of these intragranular $L1_2$ precipitates were quantita- tively determined, which were adequately characterized

by the classical Lifshitz-Slyozov-Wagner model. The activation energy for coarsening was determined to be 378 kJ/mol, which is relatively higher than that of conventional Ni or Co-based superalloys, suggesting a slow elemental diffusion in the HEA matrix. More importantly, the heterogeneous precipitation and the associated metastable phase transformation mechanism along grain boundaries (GBs) were carefully analyzed. Localized chemical heterogeneity was identified within the discontinuous $L1_2$ phase at the GBs, which thermodynamically destabilizes the $L1_2$ structure and encourages the formation of brittle Heusler phase. Finally, we establish a unique duplex-aging strategy that can be efficiently utilized for GB stabilization, by which these detrimental intergranular heterostructures can be greatly eliminated, leading to an exceptional resistance to intermediate-temperature embrittlement, along with enhanced tensile strengths. These findings will not only shed light on the precipitation mecha- nisms in compositionally complex HEAs but also generate new opportunities to the interfacial design of HEAs for advanced high-temperature applications with superior properties.

1.Introduction

The discovery of multi-component high-entropy alloys (HEAs) has opened up a new era in the development of high-performance materials for advanced structural applications [1—5]. Among them, the face-centered-cubic (FCC) HEAs strengthened by coherent L12 nanoparticles have been attracting a great interest, which are promising to provide unique solutions to the limitations imposed on conventional alloys [6—10]. By leveraging the combined merits of both the ductile multi-component matrix and precipitates, these novel L12-strengthened HEAs shows a great potential to get a superior

balance of mechanical properties across a wide temperature range [8,11,12]. He et al. [6] demonstrated that a minor addition of Ti and Al can produce a fine dispersion of L12 nano-precipitates in a FeCoNiCr-based HEA, leading to a drastic enhancement of the tensile strength. Moreover, our recent studies reveal that the L12-strengthened HEAs are able to possess excellent tensile properties at even cryogenic temperatures, showing no indication of any embrittlement [8,11,12]. A notable example was reported in the L12-strengthened FeCoNiCrTi0.2 HEA. When the temperature decreases from 293 K to 77 K, its tensile strength was increased from 1.24 to 1.58 GPa, together with a combined improvement of ductility from 36 to 46% [12]. The dynamic formation of refined stacking faults was demonstrated as an effective toughening mechanism for achieving such a large tensile ductility.

Given the similar microstructures to those of Ni-based superalloy, these newly developed L12 strengthened HEAs are considered as promising candidates for heat-resistant materials [9,13 17]. To obtain superior mechanical properties at elevated temperatures, it is critical to attain a high volume fraction of L12 precipitates with high thermal stability. Recent studies indicated that the sluggish diffusion in the multi-component matrix is conducive to improve the coarsening resistance of the L12 nanoprecipitates. For example, Zhao et al. [13] revealed that the coarsening kinetics of L12 precipitates in the (NiCoCrFe)94Al4Ti2 (at.%) HEA was much slower than that in the conventional Ni-based alloys. A similar result was also founded in the (NiCoCr)94Al3Ti3 (at.%) alloy [16]. However, these alloys typically had a small volume fraction of the L12 phase (~20%), which are only stable at the low-temperature regime (< 900℃), making them insufficient for many practical applications. Furthermore, the presence of multiple elements and associated complex chemical interactions in HEAs substantially increase the propensity for forming undesired heterogeneous precipitation of brittle intermetallic phases, especially at the GBs. The resulting intergranular embrittlement eventually sets

the most severe limits on their high-temperature applications. For example, detrimental intergranular phases, such as the Ni2(Al, Ti)-type Heusler phase, Ni3Ti-type h phase and Laves phase, have been frequently observed at the GBs in previously reported HEAs [18 21]. Minor amounts of them would not do much harm on their roomtemperature properties, which, however, cause a serious GB embrittlement of alloys at the intermediate temperatures (typically at about 600—800°C), leading to the catastrophic brittle fracture during tension deformation [22 25]. As a result, developing an effective method to suppress the formation of brittle intermetallic phases at the GBs is urgently desirable. During the past years, several thermodynamic and kinetic approaches have been explored in previous studies [26 30], which advance the optimizing design of intragranular structures. However, the ability to get a well-targeted control of GB precipitations remains extremely challenging in the complex HEAs. The significant obstacle is due to the lack of quantitative and mechanistic understanding of precipitation mechanisms governing the brittle phase formation at the GBs.

In this study, we attempt to probe the intrinsic source of the GB heterogeneous precipitation behaviors and provide new insights into the interfacial design of novel L12-strengthened HEAs towards enhanced high-temperature applications. As a result, here we mainly focus on the intrinsic thermal stability and coarsening kinetics of multi-component L12-strengthened HEAs. The Ni-30Co-13Fe-15Cr-6Al-6Ti-0.1B (at.%) HEA (referred to as Al6Ti6 HEA hereafter) was selected here as a model alloy for isothermal aging treatments at 800—1000°C from 24 to 720h. The specific objectives of this study can be described as follows: (1). To systematically characterize the temporal evolution of the intragranular L12-type precipitate isothermally aged at 800, 900 and 1000°C; (2) To quantitatively reveal the coarsening kinetics and mechanisms of the intragranular L12-type precipitate; (3) To experimentally determine and control the precipitation behaviors and phase transformation

mechanisms at the GBs. Particular attention was paid to identify the precipitation mechanisms of the discontinuous L12 phase and brittle Heusler phase at the GBs. More importantly, based on these systematical investigations, we propose a duplex-aging approach that can be effectively used to eliminate the embrittling GB heterostructures of the L12-strength-ened HEAs. Benefiting from this, enhanced microstructural stability and outstanding mechanical properties can be achieved. The present research would shed new light on the future design of L12-strength-ened HEAs for structural applications at elevated temperatures.

2. Experimental procedures

2.1 Materials preparation

The Al6Ti6 HEA with a chemical composition of Ni-30Co-13Fe-15Cr-6Al-6Ti-0.1B (in at.%) was produced by arc melting with a mix- ture of high-purity raw elements (~99.9 wt.%) in a Ti-gettered argon atmosphere. The ingots were flipped over and re-melted for at least five times to reduce the macroscopic inhomogeneity in composition and microstructure. The melted alloys were then rapidly dropped into a water-cooled copper mold with a dimension of $5 \times 12 \times 100 \mathrm{mm}^3$. The as-cast ingots were first solution-treated at 1165°C for 2h and then cold-rolled along the longitudinal direction with a total thickness reduction of ~65%, followed by recrystallization at 1165 °C for ~2 min. Subsequently, isothermal aging treatments were applied in these samples at the temperatures ranging from 800 to 1000°C for various durations (from 24 to 720 h). To avoid the damaging effects of oxidation during the long-term heat treatment, samples were encapsulated in quartz tubes filled with high-purity argon gas before aging. To avoid any potential intergranular cracks caused by water quenching, all the heat treatment procedures described here were finished by oil quenching.

2.2 Microstructural analysis

A field-emission scanning electron microscope (FE-SEM, FEI, Quanta 450) was used to image the microstructural evolution of alloys. Standard metallographic techniques were used to mount and polish heat-treated samples. The specimens were mechanically ground, pol- ished, and then followed by chemical etching for about 1min with a dilute aqua regia solution (200ml of C_2H_5OH, 75 mlof HNO_3 and 25ml of HCl) [31]. A transmission electron microscope (TEM, JEOL- 2100F) equipped with an energy dispersive spectrometer (EDS) was employed to identify the crystal structure and chemical composition of constituent phases. For the TEM investigations, the slabs were firstly mechanically ground to a thickness of about $50\mu m$ using SiC paper and then punched into 3mm diameter discs. After that, these samples were mechanically dimpled and further thinned by ion milling to a thickness of electron transparency using a precision ion polishing system (PIPS, Model 695, Gatan). Similar to coarsening studies of the gamma prime phase in superalloys, the radius of the $L1_2$ nanoparticles in this study was estimated to be a/2, where a is the mean edge length of the cubic precipitates. In order to reduce experimental errors and obtain more accurate results, over one hundred of $L1_2$-type precipitates have been measured for each aging condition. Electron backscat- ter diffraction (EBSD) measurements were performed using a FE-SEM with an Oxford detector. For the reflective EBSD tests, specimens were mechanically polished down to 1mm, followed by electropolishing in a solution of HNO_3 (25%) and C_2H_5OH (75%) with a direct voltage of 20V at the temperature around −40 °C. To obtain a high-resolution mapping of grain-boundary precipitation morphologies, transmission Kikuchi diffraction (TKD) analyses were carried out by using the TEM specimens, operated at an accelerating voltage of 30KV with a current of 0.8nA. The phase transition temperatures were examined by differential scanning calorimetry (DSC, Mettler-Toledo, Star system) under an argon atmosphere at a heating rate of 10

°C/min.

Elemental distribution at atomic scales was determined using a local electrode atom probe tomography (APT, CAMEACA LEAP 5000 XR). Tip-shaped specimens for the APT test were fabricated by a liftout method and annularly milled in a focused ion beam/scanning electron microscope (FIB/SEM, FEI Scios). The APT specimens were analyzed at 70K in the voltage mode, with a pulse repetition rate of 200 KHz, a pulse fraction of 20%, and an evaporation detection rate of 0.2% atom per pulse. After that, Imago Visualization and Analysis Software (IVAS) in version 3.8.2 was used for 3D reconstruction and composition analysis.

2.3 Mechanical tests

Dog-bone-shaped specimens with a gauge length of 12.5 mm and a cross-section dimension of $3.2 \times 1.5 \text{mm}^2$ were fabricated by elec-tro-discharge machining (Sodick, AQ360LX) for tensile tests. Both sides of the specimens were carefully ground to 2500-grit finish using SiC paper. The uniaxial tensile tests were performed on a Material Testing System (MTS) tension machine at ambient and elevated temperatures with a strain rate of $1 \times 10^{-3} \text{s}^{-1}$. Temperature was monitored by using three K-type thermocouples.

2.4 Theoretical calculations

Thermodynamic calculations were conducted by using the software of Thermo Calc 3.0.1 based on a Ni-based database (TTNI8). Energetics of various binary $L1_2$-type structures were studied by the first-principles calculations using the density-functional theory (DFT) implemented in the Vienna ab initio Simulation Package (VASP). The Coulomb interaction of ion cores with the valence electrons and the electronic exchange were described by Projector-augmented wave potential and the Per-dew Burke

Ernzerhof generalized gradient approximation, respectively. Three-dimensional 4 atom periodic unit cells were used to determine the total energy by using the $9 \times 9 \times 9\Gamma$ centered Mon-khorst-Pack meshes with a plane wave energy cutoff of 500eV. Equilibrium cell volumes and internal atomic positions of the supercells were fully relaxed until the total energy differences $< 10^{-4}$ eV.

3. Results

3.1 Microstructures of the as-solutionized sample

Fig. 1(a) shows the electron backscatter diffraction (EBSD) mapping of the solid-solution-treated Al6Ti6 HEA after the oil quenching. A fully recrystallized microstructure with an average grain size of $40\mu m$ can be clearly observed. Fig. 1(b) presents a close-up view of the GBs. It appears that no measurable precipitation can be observed in the assolutionized sample. Fig. 1(c) shows a reprehensive dark-field TEM (DF-TEM) image, revealing the presence of nanoprecipitates with an average size of about 13±2nm. Selected area diffraction patterns (SADP) took along the [001] zone axis (inset in Fig. 1(c)) show the superlattice spots, indicating that a $L1_2$ ordered phase has formed during the cooling process. This result indicates a rapid precipitation kinetic of these $L1_2$ precipitates in the present HEA system. Given the extremely fine sizes of these $L1_2$ precipitates, determination of the chemical composition via the EDS technique would lead to a considerable error. As a result, needle-shaped tips were lifted out from the sample and subsequently analyzed by APT, by which the chemistries of nanophases can be quantitatively determined. Atom maps and corresponding proximity histogram across the matrix/particle interfaces are presented in Fig. 1(d) and (e), respectively. The average size of the $L1_2$ phase can be estimated to be about 12 nm, which agrees well with the TEM analysis (Fig.

1(c)). Apparently, from Fig. 1(e), we can see that Ti, Al and Ni have a very strong tendency to partition into the $L1_2$ nanoparticles, while Co is partially depleted, and Cr is largely depleted from the nanoparticles, which agrees well with previous studies [6,32]. This result further proof that these second-phase nanoparticles are $L1_2$ precipitates with a distinct chemical composition compared to the FCC matrix, rather than the equi-composition $L1_2$ ordered zones due to congruent ordering during quench [33]. Based on these analy- ses, these $L1_2$-type nanoparticles can be consequently identified as the ordered $(Ni,Co,Fe,Cr)_3(Ti,Al)$ phase with a volume fraction of about 24% by using the lever rule [34].

3.2 Temporal evolutions of the intragranular L12-type precipitates

Fig. 2 shows the representative SEM images of samples isothermally aged at 800°C, 900°C and 1000°C for different time intervals. It is evident that the intragranular microstructures of the aged samples under this temperature range were essentially dominated by the uniform precipitation of the $L1_2$ phase embedded in the FCC matrix. The chemical compositions of the 720h aged sample, which can be regarded as the equilibrium states, were evaluated by TEM-EDS and summarized in Table 1. The ordering nature of the precipitates was confirmed via TEM analysis. For example, a selected DF-TEM micrograph and the corresponding SADP of the precipitate in alloys aged at 800°C for 720h were presented in Fig. 3(a) and (b), respectively. The ordered $L1_2$ structure can be clearly evidenced, without precipitation of other intermetallic phases in the grain interiors. Fig. 3(c) clearly demonstrates that these cuboidal precipitates are Ni-and Al-and Ti- rich while the matrix is enriched with Fe, Co and Cr, which can be identified as the $(Ni,Co,Fe,Cr)_3(Ti,Al)$-type phase. Furthermore, the coarsening behaviors

of these intragranular $L1_2$ precipitates were investigated via detailed characterizations on the temporal evolutions of the morphology and particle size during isothermal aging treatment. Despite ellipse shapes at an early stage of growth at 800°C , it is evident that all the $L1_2$ precipitates kept cuboidal after longterm aging (Fig. 2(c) and (d)), especially at higher temperatures of 900 (Fig. 2(e) (h)) and 1000°C (Fig. 2(i) (l)), implying that a relatively large lattice misfit may exist between the precipitate and the matrix. As shown in Fig. 4and Table 2, the average sizes of $L1_2$ precipitates gradually increase with the increase of aging durations and temperatures. For samples aged for 720h, when the temperature increases 800—1000°C, the average sizes of the $L1_2$ precipitates were 93.7, 308.3 and 780.4 nm, respectively. Correspondingly, the volume fraction of the $L1_2$ precipitates gradually decreases from ~37% to 17%, respectively.

3.3 Microstructural evolution at the GBs upon aging

Fig. 5 shows representative SEM images of the alloys after 720h of aging at 800—1000°C. The grain interiors of all three samples maintain the dual-phase "$L1_2$+FCC" microstructure. However, a significant difference in the GB morphologies can be clearly identified. Samples aged at 800 and 900°C exhibit a similar precipitation behavior at the GBs. In addition to the fine $L1_2$-type precipitates, blocky particles with micron sizes were observed to form at the GBs region (marked by arrows in Fig. 5 (a) and (b)). In contrast, the sample aged at 1000°C exhibits excellent microstructural stability, retaining a pristine "$L1_2$ + FCC" dual-phase structure at the GBs with no measurable precipitation of other intermetallic compounds, as shown in Fig. 5 (c).

TKD and TEM analyses were further conducted to determine the crystalline structure of these blocky particles, as shown in Fig. 5 (d) and (e). Different from the $L1_2$ precipitates with an ordered FCC

structure, these blocky particles have an ordered body-centered-cubic (BCC) structure. Furthermore, additional TEM studies of the SADP identify them as the $L2_1$-type (a highly ordered BCC structure) Heusler phase with a lattice constant of 0.59nm (Fig. 5 (e)), and the corresponding scanning TEM EDS (STEM-EDS) indicates that these large particles are enriched in Ni, Co, Al and Ti. Similar results have also been achieved in the sample aged at 900°C, and the detailed microstructural information on the GB Heusler phase was summarized in Table 1. The volume fractions of the GB Heusler phase for the specimens isothermally aged at 800 and 900°C can be estimated to be around 0.87% and 1.19%, respectively. Such a Heusler-like $L2_1$ phase was also frequently in other HEAs with various Ti and Al contents, for example, the $(FeNiCoCr)_{1-x-y}Ti_xAl_y$ [6,18] and CoCrCuFeNiAlTi HEAs [35,36]. This kind of highly ordered Heusler phase is extremely brittle and incoherent with the FCC HEA matrix, the formation of which, especially at GBs, causes increased local stress concentration and associated brittleness of alloys [18]. The precipitation mechanism of the GB Heusler phase will be carefully discussed in the next section.

4. Discussion

The above experimental results show that the non-equiatomic Ni-Co-Fe-Cr-based HEA with relatively high Al and Ti concentrations exhibit pronounced precipitation of the coherent ordered $L1_2$ precipitates at elevated temperatures, which is crucial for maintaining the strengths at high-temperatures. In the following sections, we will discuss in more detail the coarsening kinetics of the L12-precipi-tates in the studied HEA. Furthermore, a special emphasis will be put on the GB precipitation behavior, aiming at elucidating key factors governing the precipitation of brittle Heusler phase at the GBs.

4.1 Coarsening kinetics of the intragranular L1$_2$-type precipitate

The coarsening kinetics and associated mechanisms of the L1$_2$- type precipitates in the FCC matrix have been extensively studied, especially in cases of superalloys. Most of the previous studies demonstrated that the coarsening behaviors of the L1$_2$ precipitates are basically governed by the solute diffusion through the matrix, which can be described as the classical Ostwald ripening process based on the theory proposed by Lifshitz, Slyozov and Wagner (LSW theory) [37]. Such a time-dependent coarsening process can be described following the power-law expression,

$$r^3(t) - r^3(t_0) = k(t - t_0)$$
（1）

where r(t) is the average size of precipitate at the aging time of t.k is the coarsening rate constant, which is largely dependent on the diffusion of the solute and the interfacial energy between the precipitates and matrix. More recently, Philippe and Voohees expanded the LSW theory to a multi-component system by taking advantage of the increasingly available computational thermodynamic and diffusion data [38]. Given that a low mobility specie in a complex multi-com-ponent alloy would govern the coarsening kinetics of the average precipitate radius [39], the coarsening rate constant of the L1$_2$ precipitate can be expressed as following

$$k \approx \frac{8 V_m \sigma D c_i^M}{9RT \left(c_i^P - c_i^M \right)^2}$$
（2）

where V_m is molar volume of the matrix, σ is the precipitate/matrix interfacial energy, c_i^M, c_i^P are the equilibrium composition (in mole fraction) of the element i in the prectipitates and matrix, respectively, R is the gas constant ($= 8.31 J\ mol^{-1}\ K^{-1}$). T is the absolute temperature. D is the diffusion coefficient of the slow element in the matrix, which can be further extended following the Arrhenius

expression:

$$D = D_0 \exp\left(\frac{-Q}{RT}\right) \tag{3}$$

in which D_0 is the pre-exponential factor and Q is the activation energy of the diffusion. The measured equilibrium radius, is plotted with the variation of aging time in Fig. 6. The experimental data appear to be well fifitted with the LSW model. According to Eq. (1), linear fifits to these plots for the respective datasets yield slopes that give the rate contants, $k = 3.46 \times 10^{-29} m^3 / s$ $1.4 \times 10^{-27} m^3 / s$ and $2.25 \times 10^{-26} m^3 / s$ for 800℃ , 900℃, respectively. It is evident that the coarsening rates gradually increase with the increase of aging temperatures. The coarsening rates of Al6Ti6 are relatively lower than those of many other reported Ni and Co-based superalloys which generally contain higher amounts of slow diffusing elements such as W, Mo or Re [16,40]. Assuming that Vm and the equilibrium concentration in both matrix and the precipitates are weakly temper-ature-dependent, fifitting Eq. (3) yields an activation energy of 378 kJ/mol for the present case. It is interestingly to note that this value is relatively higher than those activation energies for most solutes in Ni-and Co-based alloys, as summarized in Table 3, with their apparent range being 254-289kJ/mol [13,41,42]. In general, the higher activation energy suggests a higher diffusion barrier of vacancy formation and migration for the diffusion species in the current multicomponent FCC matrix, which is consistent with the proposed nature of sluggish diffusion in the HEAs in previous literature [13,16,42]. From the point of view of diffusion, the larger activation energy is conducive to retard the coarsening of precipitates. As a result, it is safe for us to conclude that the excellent coarsening resistance of the current HEA is primarily ascribed to the large activation energy for elemental diffusion.

Table 3 Activation energies for diffusion in several Ni-based, Co-based alloys and high entropy alloys.

Diffusion couple or alloy	Method of measurements	Q (kJ/mol)	Ref.
Ti in Ni	Diffusion couple	275	[13]
Al in Ni	Diffusion couple	268	[13]
Co in Ni	Diffusion couple	284	[41]
Fe in Ni	Diffusion couple	269	[41]
Cr in Ni	Diffusion couple	289	[41]
Ti in Co	Diffusion couple	262	[38]
Al in Co	Diffusion couple	281	[38]
Ni in Co	Diffusion couple	282	[41]
Fe in Co	Diffusion couple	263	[41]
Cr in Co	Diffusion couple	254	[41]
Ni-13.5Al	Precipitation coarsening	270	[13]
Ni-10.5Ti	Precipitation coarsening	283	[13]
Ni-6.5Ti-4.5Al	Precipitation coarsening	285	[13]
Nimonic 105	Precipitation coarsening	264	[13]

Nimonic 90	Precipitation coarsening	257	[13]
(FeCoNiCr)$_{94}$Al$_4$Ti$_2$	Precipitation coarsening	276	[13]
Present HEA	Precipitation coarsening	378	—

It is worthy mentioning that the coarsening rate at 800°C of the Al6Ti6 HEA is slightly faster than some of recently reported HEAs, such as the (NiCoCr)Al$_3$Ti$_3$ alloy ($1.23\times10^{-29}\,\text{m}^3/\text{s}$) and (FeCoNiCr)94Al$_4Ti_2$ alloy $(2.26\times10^{-29}\,\text{m}^3/\text{s})$ [16]. According to Eq. (2), the coarsening rate is a collective effect from the diffusion of the slowest species and the precipitate/matrix interfacial energy. It is well known that the equilibrium shape of the coherent L1$_2$ precipitate is governed by the total energy minimization, involving contributions from interfacial energy and elastic energy. Thompson et al. [43] proposed a parameter $L=\varepsilon^2 C_{44} r/\sigma$ to describe the equilibrium morphology of a particle, where e is the lattice mismatch strain, which can be estimated to be 0.41% by XRD (not shown here) for the 800°C aged sample. C44 is an elastic constant of the matrix. A C$_{44}$ of 124 GPa, borrowed from Ni-based superalloys [44], will be used in the present case. As indicated in the Thompson's theory, the four-fold symmetry shape is energy minima for L < 5.6, above which a two-fold precipitate shape will be more energetically favored. Since the shape of the precipitates in the current HEA are mostly remains cuboidal (as shown in Fig. 2), L=5.6 can be used to estimate the lower bound of the interfacial energy for the present HEA. Substituting the experi- mentally determined values, the interfacial energy was estimated to be about 40 mJ/m^2 for the samples aged at 800°C, which is significantly higher than that of the NiCoCr (~4 mJ/m^2) [16]. The relatively larger interfacial energy would increase the coarsening kinetics of the current HEA to some extent, though it may be restricted by the higher diffusion barrier. It can be expected that the coarsening resis- tance would be improved further by

reducing the interfacial energy through compositional optimization.

4.2 Mechanisms for the precipitation of Heusler phase at the GBs

As shown in a former section, upon aging at 800—1000°C, drastic changes in morphology and microstructure of the GBs are evidenced experimentally. In the following section, we will discuss in detail the underlying origins of the heterogeneous precipitation of the brittle precipitates, which is essential for the exploration of avenues to eliminate the GB embrittlement. Given the similar GB precipitation behaviors in the alloys aged at 800 and 900°C (as shown in Fig. 5), for clarity and simplicity, we mainly focus on the discussion of Heus- ler phase formation in the 800°C aged alloy.

To better understand the precipitation pathway of the Heusler phase, we prepared the sample aged at 800°C for 4 h, and the microstructures were carefully analyzed and presented in Fig. 7. It is interesting to note that no GB-precipitated Heusler phase can be identified at the early stage of aging. The GB region is dominated by the discontinuous precipitation of $L1_2$ precipitates with a cellular shape, as shown in Fig. 7(a)—(c). As shown in Fig. 1, owing to the coherent relationship with the FCC matrix, it is the $L1_2$ phase, rather than the Heusler phase, that first nucleates and comes out of the initial solid solution. As a result, the heterogenous precipitation of cellular $L1_2$ phase at the GBs during the isothermal aging at 800°C can be ascribed to a discontinuous-coarsening mechanism, wherein the prior coherent matrix-precipitate structure gradually transforms into the coarser lamellae structure [45]. Previous studies suggest that the discontinuous precipitation reaction requires the movement of GBs, which is essentially driven by the compositional supersaturation of $L1_2$-forming elements in the FCC matrix, especially the Ti and Al [32,46,47]. However, up to date, there is no direct
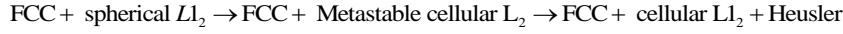
experimental evidence to support this assumption. Noticeably, as shown in Fig. 7(d) and (e), we experimentally revealed that the cellular L1$_2$ precipitates exhibit a markedly compositional heterogeneity, showing the localized enrichments of Ni, Ti, and Al elements accompanied with depletion of Fe and Cr elements at the GB region. The closer to the GBs, the stronger supersaturations of Ni, Ti and Al can be clearly observed. In comparison, the FCC matrix is compositionally homogenous with a random distribution of all elements (as shown in *Supplementary Fig. 1)*. It suggests that it is the chemical inhomogeneity within the cellu- lar L1$_2$ precipitates, instead of the FCC matrix, that governs the reac- tion of discontinuous precipitation at the GBs. From an energetic standpoint, the localized chemical variations provide the basic chem- ical driving force for the movement of GBs as well as the growth of discontinuous precipitation [45]. Meanwhile, as compared to the Ni, Co, Fe, and Cr elements with the similar atomic radius (about $1.24-1.28\text{Å}$ [31]), the Ti and Al elements have larger atomic sizes ($r_{Ti}=1.47\text{Å}, r_{Al}=1.43\text{Å}$ [40]), the localized supersaturations of them will also lead to the increased particle/matrix mismatch, which causes an enhanced strain energy of the surrounding FCC matrix and thus promotes the formation of discontinuous L1$_2$ phases at the GBs [45]. In addition, diffusion along the GBs at 800°C is expected to be much faster than that of the bulk lattice within the grain interiors, which will kinetically promote the discontinuous growth of cellular L1$_2$ phase [18,32,45,48,49].

The oriented compositional enrichments of Ni, Ti and Al can be qualitatively rationalized in terms of the elemental segregation at the local regions of GBs. Murdoch [50] developed a Miedema-type segregation model, by which the propensity for segregation of elements at the GBs can be estimated. Specifically, in the Ni-X solid-solution systems, Ti and Al elements show positive values of segregation enthalpy (ΔH_{seg}), suggesting that the Ti and Al atoms are energetically favored to segre- gate to the GBs.

Moreover, the larger differences in atomic sizes as com- pared with the matrix elements of Ni, Co, Fe and Cr may also make the Ti and Al atoms favorable to migrate to the loosely packed regions like GBs [51]. Furthermore, by using the DFT calculations, we revealed the intrinsic energetic differences between various binary $L1_2$-type sus-sys- tems with different atomic pairs, as shown in Fig. 8(a). As can be seen, the formation energies of Ni_3Ti and Ni_3Al were determined to be about —0.475 and —0.422eV/atom, respectively, which are more negative than those of other binary $L1_2$ structures. These calculated results imply that the formation (Ni, Ti, Al)-enriched $L1_2$-type is thermodynamically favored at the very early stage of aging, leading to the pronounced enrichments of Ni, Ti and Al at the advancing GBs, which is in good con- sistency with our STEM-EDS observations.

Furthermore, higher Ti and Al supersaturations play an important role in the subsequent phase transformation behavior, which will thermodynamically destabilize the cellular $L1_2$ precipitates and induce the formation of Heusler phase at the later stage of aging. Our thermodynamic calculations provide a fundamental understanding of such a supersaturation-induced phase transition. As presented in Fig. 8(b), we calculated the isothermal phase diagram of the Ni-Co-Al-Ti system (major elements supersaturated in the cellular $L1_2$ phase) at the aging temperature of 800°C， which shows the effects of Al and Ti additions on the thermodynamic stability of the $L1_2$ phase. It is evident that the increased supersaturation of Ti and Al thermodynamically destabilize the $L1_2$ structure, which in turn promotes the formation of BCC-type Heusler phase locally stabilized at the GBs. A recent work by Choudhuri et al. [36] also suggests that the Ti element is essential to promote the stabilization $L2_1$ phase in the $Co_{0.5}CrCu_{0.5}FeNi_{1.5}AlTi_{0.4}$ HEA based on the DFT calculations. Taken together, the complex precipitation pathway at the GBs of the sample isothermally at 800°C can be summarized as follows: (1) A rapid precipitation of the $L1_2$ phase during the oil quenching process from the initial concentrated solid solution; (2) A subsequent discontinuous precipitation and growth

of the metastable L1$_2$ precipitates at the GBs within the early aging stage; (3) As the precipitation reaction

continues, the destabilization of cellular L1$_2$ phase occurs, leading to the formation of the brittle Heusler

phase locally stabilized at GBs. As schematically illustrated in Fig. 8(c), the precipitation sequence can be

expressed as:

$$\text{FCC} + \text{ spherical } L1_2 \rightarrow \text{FCC} + \text{ Metastable cellular } L1_2 \rightarrow \text{FCC} + \text{ cellular L1}_2 + \text{Heusler}$$

In contrast, the sample aged at 1000°C exhibits no precipitation of the brittle Heuser phase at GBs. This

could be ascribed to the reduced segregation at GBs under such a high aging temperature. The compositional

segregation to the GBs can be estimated by the McLean's model [52]:

$$\frac{C_{gb}}{1-C_{gb}} = \frac{C_{gi}}{1-C_{gi}} \exp\left(\frac{\Delta H_{seg}}{RT}\right)$$ （4）

where C_{gb} and C_{gi} are the solute concentrations at the GBs and in the grain interior, respectively, and

ΔH_{seg} is the segregation enthalpy, T is the temperature, R is gas constant. According to Eq. (4), it is

evident that the elemental concentrations segregated at GBs will decrease with the increase of aging

temperature, which thereby inhibits the nucleation of the Heusler phase. On the other hand, as the

temperature increases, the lattice diffusion becomes faster, and the GB diffusion will become less

pronounced, which thermodynamically favors the continuous precipitation of L1$_2$ phase [45,49]. The

chemical driving energy available for both the initiation and propagation of discontinuous precipitates

will be reduced accordingly, resulting in the disappearance of cellular L1$_2$ phase at GBs. It was

generally found that the lattice diffusion becomes dominant at temperatures above about 0.75-0.8T$_m$,

where T$_m$ is the melting temperature of the alloy [53]. By using the DSC method, the initial melting

temperature of our present HEA can be determined to be about 1270°C (not shown here). This means

that the lattice diffusion becomes more pronounced at the temperature higher than 953-1016°C, which agrees well with our experimental results.

4.3 Duplex-aged design for GB stabilization

Detrimental precipitation of heterostructures involving the discontinuous $L1_2$ phase and Heusler phase at the GBs have long been associated with property reduction as sites for crack initiation and propagation, which severely weaken the GBs of HEAs, leading to the brittle intergranular fracture during the tensile deformation [23,24,46,54]. Such an undesired precipitation behavior has also been frequently observed in many HEAs systems, which are generally recognized as a stable structure that can be suppressed only by compositional adjustments. In contrast, based on the above analyses, we demonstrated that the formation of GB heterostructures is primarily governed by the localized chemical instability and diffusional heterogeneity in the vicinity of GBs. With this understanding, here we proposed a duplex-aged design that potentially enables the stabilization of GBs in multi-component $L1_2$-strengthened HEAs, as schematically illustrated in Fig. 9(a). The underlying wisdom of this strategy can be described as: (a) Sub-solvus aging treatment at the temperature of about 0.75—$0.8T_m$ to promote continuous precipitation at the GBs. The preformed cuboidal $L1_2$ precipitates generate a strong particlepinning effect, which significantly retards the migration of GBs and then inhibits the formation of cellular $L1_2$ phases at the GBs. (b) Secondary aging treatment at lower temperatures to introduce a higher volume fraction of the $L1_2$ phase, which is vital for maintaining a high level of strength. As a proof-of-concept implementation, a duplex-aged Al6Ti6 HEA was prepared by aging at 1000°C for 4h and then 800°C for 24h. As shown in Fig. 9(b) and (c), in comparison to the sample aged at 800°C for 24h, two distinct changes can be clearly observed: (a) a complete removal of the discontinuous precipitation; (b) a thorough elimination of the brittle Heusler phase. The structure of the GBs is almost

the same with that of the grain interior, which is dominated by the uniform precipitation of $L1_2$ particles with a bimodal size distribution (Fig. 9(d) and (e)). The average sizes of the precipitates can be determined to be about 145±30nm and 36±5nm, respectively. To evaluate the effects of the GB structures on the intermediate-temperature   properties of the investigated HEAs, uniaxial tensile tests were conducted at 700°C—a crucial tem- perature capability for turbine disk materials [55]. Remarkably, as shown in Fig. 10(a), a distinct brittle-to-ductile transition can be readily observed from these HEAs with different GB features. The one-step aged samples exhibit brittle GB fractures with poor tensile ductilities (~3%), exhibiting the typical cleavage GB facets together with intergranular cracks (Fig. 10(b)). Evidently, the heterogeneous precipitations of both the cellular $L1_2$ precipitates and Heusler phase cause serious embrittlement of the GBs. Similar results have also been reported in previous studies [32,46,54]. In contrast, the duplexaging treatment significantly suppresses the formation of these undesired GB heterostructures and effectively eliminates the GB embrittlement, leading to a twofold enhancement of tensile ductility. Meanwhile, as shown in Fig. 10(b), a fully ductile facture surface dominated by pronounced dimples can be clearly identified. More importantly, a combined increase rather than a decrease of tensile strength can be obtained with such a ductilization process, which is crucial for the elevated temperature applications of alloys. A direct comparison of the tensile strength as a function of temperature between our present HEA and other reported conventional alloys and HEAs was also presented in Supplementary Fig. *2* [9], showing a great potential of our present HEA for high-temperature applications.

Overall, we unveiled the metastable nature of the GB precipitation and demonstrated a new avenue to tailor the localized nanostructures at the GBs of HEAs. It is eminently feasible that mechanical properties of present HEAs can be improved further by optimizing the aging parameters

in the future. The exciting results achieved in this work also lend to our credence that the duplex-aging design strategy will generate new opportunities to many other complex alloys for the GB stabilization, especially for those that the formation of brittle intermetallic phases at GBs must be suppressed.

5. Conclusion

The thermal stability of a $L1_2$-strengthened Ni-30Co-13Fe-15Cr-6Al-6Ti-0.1B (at.%) HEA aged at 800—1000°C has been systematically investigated. Coarsening kinetics of the intragranular $L1_2$ precipitates and the phase transformation behaviors at the GBs were carefully characterized by combining APT, EBSD, TEM and SEM. The thermodynamic analyses and the DFT calculations provide the fundamental understandings of the complex precipitation mechanisms, which is crucial for the well-targeted control of nanoprecipitation in multicomponent HEAs. Based on our observations, some key conclusions can be drawn as follows:

(a) Ordered $L1_2$ nanoparticles are rapidly precipitated out from the concentrated solid solution during the oil quenching, which shows a distinct composition with regard to the FCC matrix.

(b) The microstructures in the grain interiors are essentially dominated by the uniform precipitation of coherent $L1_2$ phase embedded in the FCC matrix. The coarsening kinetics were adequately characterized by the classical LSW theory. The activation energy of $L1_2$ precipitate coarsening can be estimated to be about 378 kJ/mol,   which is significantly higher than that of conventional Ni- or Co-based superalloys, suggesting a relatively   sluggish diffusion in the multi-component FCC matrix.

(c) The precipitation behavior at the GBs shows a strong temperature dependence. Formation of the

brittle Heusler phase is favored at lower aging temperatures, which is highly related to the localized compositional variations and diffusional heterogeneities at the GBs. TEM results reveal a strong enrichment of Ti and Al within the GB cellular $L1_2$ phases, which thermodynami- cally destabilizes the $L1_2$ structure, promoting the phase transformation into the ordered-BCC Heusler phase.

(d) We innovatively propose a duplex-aging design that allows a general rule to controllably tailor the local nanostructures at the GBs for GB stabilization. Leveraging on this strategy, the embrit- tling intergranular heterostructures can be greatly eliminated, leading to a distinct brittle-to-ductile transition at the intermedi-ate-temperature of 700°C associated with a combined increase of tensile strengths up to 1.0GPa. This approach is expected to be efficiently applied to many other alloys systems, especially for those with similar microstructures.

Declaration of Competing Interest

Acknowledgments

References

[1] J.W. Yeh, S.K. Chen, S.J. Lin, J.Y. Gan, T.S. Chin, T.T. Shun, C.H. Tsau, S.Y. Chang, Nanostructured high entropy alloys with multiple principal elements: novel alloy design concepts and outcomes, Adv. Eng. Mater. 6 (5) (2004) 299–303.

[2] B. Gludovatz, A. Hohenwarter, D. Catoor, E.H. Chang, E.P. George, R.O. Ritchie, A fracture-resistant high-entropy alloy for cryogenic applications, Science 345 (6201) (2014) 1153–1158.

[3] Z. Li, K.G. Pradeep, Y. Deng, D. Raabe, C.C. Tasan, Metastable high-entropy dual- phase alloys overcome the strength-ductility trade-off, Nature 534 (7606) (2016) 227–230.

[4] Z. Lei, X. Liu, Y. Wu, H. Wang, S. Jiang, S. Wang, X. Hui, Y. Wu, B. Gault, P. Kontis, Enhanced strength and ductility in a high-entropy alloy via ordered oxygen com- plexes, Nature 563 (7732) (2018) 546.

[5] Z. Wang, I. Baker, Z. Cai, S. Chen, J.D. Poplawsky, W. Guo, The effect of interstitial carbon on the mechanical properties and dislocation substructure evolution in Fe40.4Ni11.3Mn34.8Al7.5Cr6 high entropy alloys, Acta Mater. 120 (2016) 228– 239.

[6] J.Y. He, H. Wang, H.L. Huang, X.D. Xu, M.W. Chen, Y. Wu, X.J. Liu, T.G. Nieh, K. An, Z.P. Lu, A precipitation-hardened high-entropy alloy with outstanding tensile properties, Acta Mater. 102 (2016) 187–196.

[7]T. Yang, Y. Zhao, Y. Tong, Z. Jiao, J. Wei, J. Cai, X. Han, D. Chen, A. Hu, J. Kai, Multi- component intermetallic nanoparticles and superb mechanical behaviors of com- plex alloys, Science 362 (6417) (2018) 933–937.

[8]T. Yang, Y. Zhao, W. Liu, J. Kai, C. Liu, L12-strengthened high-entropy alloys for advanced structural applications, J. Mater. Res. 33 (19) (2018) 2983–2997.

[9] J. Chen, X. Zhou, W. Wang, B. Liu, Y. Lv, W. Yang, D. Xu, Y. Liu, A review on funda- mental of high entropy alloys with promising high temperature properties, J. Alloy. Compd. 760 (2018) 15–30.

[10]Y.J. Liang, L. Wang, Y. Wen, B. Cheng, Q. Wu, T. Cao, Q. Xiao, Y. Xue, G. Sha, Y. Wang, Y. Ren, X. Li, L. Wang, F. Wang, H. Cai, High-content ductile coherent nanoprecipitates achieve ultrastrong high-entropy alloys, Nat. Commun. 9 (1) (2018) 4063.

[11] T. Yang, Y.L. Zhao, J.H. Luan, B. Han, J. Wei, J.J. Kai, C.T. Liu, Nanoparticles-strength- ened high-entropy alloys for cryogenic applications showing an exceptional strength-ductility synergy, Scr. Mater. 164 (2019) 30–35.

[12]Y. Tong, D. Chen, B. Han, J. Wang, R. Feng, T. Yang, C. Zhao, Y.L. Zhao, W. Guo,

Y. Shimizu, C.T. Liu, P.K. Liaw, K. Inoue, Y. Nagai, A. Hu, J.J. Kai, Outstanding tensile properties of a precipitation-strengthened FeCoNiCrTi0.2 high-entropy alloy at room and cryogenic temperatures, Acta Mater. 165 (2019) 228–240.

[13]Y.Y. Zhao, H.W. Chen, Z.P. Lu, T.G. Nieh, Thermal stability and coarsening of coher- ent particles in a precipitation-hardened (NiCoFeCr) 94 Ti 2 Al 4 high-entropy alloy, Acta Mater. 147 (2018) 184–194.

[14]T.K. Tsao, A.C. Yeh, C.M. Kuo, K. Kakehi, H. Murakami, J.W. Yeh, S.R. Jian, The high temperature tensile and creep behaviors of high entropy superalloy, Sci. Rep. 7   (1) (2017)

12658.

[15]A. Manzoni, S. Singh, H. Daoud, R. Popp, R. Völkl, U. Glatzel, N. Wanderka, On the path to optimizing the Al-Co-Cr-Cu-Fe-Ni-Ti high entropy alloy family for high temperature applications, Entropy 18 (12) (2016) 104.

[16]Y. Zhao, T. Yang, B. Han, J. Luan, D. Chen, W. Kai, C.T. Liu, J.-J. Kai, Exceptional nanostructure stability and its origins in the CoCrNi-based precipitation-strength- ened medium-entropy alloy, Mater. Res. Lett. 7 (4) (2019) 152–158.

[17]S. Praveen, H.S. Kim, High-entropy alloys: potential candidates for high-tempera- ture applications - an overview, Adv. Eng. Mater. 20 (1) (2018).

[18]J.Y. He, H. Wang, Y. Wu, X.J. Liu, H.H. Mao, T.G. Nieh, Z.P. Lu, Precipitation behavior and its effects on tensile properties of FeCoNiCr high-entropy alloys, Intermetallics 79 (2016) 41–52.

[19]Y.-J. Chang, A.-C. Yeh, The evolution of microstructures and high temperature properties of AlxCo1.5CrFeNi1.5Tiy high entropy alloys, J. Alloy. Compd. 653 (2015) 379–385.

[20]S. Antonov, M. Detrois, S. Tin, Design of novel precipitate-strengthened Al-Co-Cr- Fe-Nb-Ni high-entropy superalloys, Metall. Mater. Trans. A 49 (1) (2017) 305– 320.

[21]Y.L. Zhao, T. Yang, J.H. Zhu, D. Chen, Y. Yang, A. Hu, C.T. Liu, J.J. Kai, Development of high-strength Co-free high-entropy alloys hardened by nanosized precipitates, Scr. Mater. 148 (2018) 51– 55.

[22]W.Z. Wang, H.U. Hong, I.S. Kim, B.G. Choi, H.W. Jeong, M.Y. Kim, C.Y. Jo, Influence of γ and grain boundary carbide on tensile fracture behaviors of nimonic 263, Mater. Sci. Eng. A 523 (1 2)

(2009) 242–245.

[23]H.-J. Chung, J.-Y. Huh, W.-S. Jung, Intermediate temperature brittleness of Ni based superalloy nimonic263, Mater. Charact. 140 (2018) 9–14.

[24]L. Jiang, X. Ye, C. Cui, H. Huang, B. Leng, Z. Li, X. Zhou, Intermediate temperature embrittlement of one new Ni-26W-6Cr based superalloy for molten salt reactors, Mater. Sci. Eng. A 668 (2016) 137–145.

[25]E. Pu, W. Zheng, Z. Song, H. Feng, F. Yang, H. Dong, Effects of temperature and strain rate on tensile deformation behavior of superalloy UNS N10276, Mater. Sci. Eng. A 699 (2017) 88–98.

[26]Y. Zhang, X. Yang, P.K. Liaw, Alloy design and properties optimization of high- entropy alloys, JOM 64 (7) (2012) 830–838.

[27]Y.F. Ye, C.T. Liu, Y. Yang, A geometric model for intrinsic residual strain and phase stability in high entropy alloys, Acta Mater. 94 (2015) 152–161.

[28]Y.P. Wang, B.S. Li, H.Z. Fu, Solid solution or intermetallics in a high-entropy alloy, Adv. Eng. Mater. 11 (8) (2009) 641–644.

[29]F. Otto, Y. Yang, H. Bei, E.P. George, Relative effects of enthalpy and entropy on the phase stability of equiatomic high-entropy alloys, Acta Mater. 61 (7) (2013) 2628–2638.

[30]O.N. Senkov, J.D. Miller, D.B. Miracle, C. Woodward, Accelerated exploration of multi-principal element alloys with solid solution phases, Nat. Commun. 6 (2015) 6529.

[31]T. Yang, Y.L. Zhao, W.H. Liu, J.H. Zhu, J.J. Kai, C.T. Liu, Ductilizing brittle high- entropy alloys via tailoring valence electron concentrations of precipitates by controlled elemental partitioning, Mater.

Res. Lett. 6 (10) (2018) 600–606.

[32]Y.L. Zhao, T. Yang, Y. Tong, J. Wang, J.H. Luan, Z.B. Jiao, D. Chen, Y. Yang, A. Hu, C.T. Liu, J.J. Kai, Heterogeneous precipitation behavior and stacking-fault-medi- ated deformation in a CoCrNi-based medium-entropy alloy, Acta Mater. 138 (2017) 72–82.

[33]A. Azzam, T. Philippe, A. Hauet, F. Danoix, D. Locq, P. Caron, D. Blavette, Kinetics pathway of precipitation in model Co-Al-W superalloy, Acta Mater. 145 (2018) 377–387.

[34]D.J. Sauza, D.C. Dunand, R.D. Noebe, D.N. Seidman, g'-(L12) precipitate evolution during isothermal aging of a Co Al W Ni superalloy, Acta Mater. 164 (2019) 654– 662.

[35] S. Liu, P. Cao, D.-Y. Lin, F. Tian, Stability of L21 (NiM)2TiAl (M=Co, Fe) in high- entropy alloys, J. Alloy. Compd. 764 (2018) 650–655.

[36]D. Choudhuri, T. Alam, T. Borkar, B. Gwalani, A.S. Mantri, S.G. Srinivasan, M.A. Gibson, R. Banerjee, Formation of a Huesler-like L21 phase in a CoCrCuFe-NiAlTi high-entropy alloy, Scr. Mater. 100 (2015) 36–39.

[37]I.M. Lifshitz, V.V. Slyozov, The kinetics of precipitation from supersaturated solid solutions, J. Phys. Chem. Solids 19 (1 2) (1961) 35–50.

[38]T. Philippe, P.W. Voorhees, Ostwald ripening in multicomponent alloys, Acta Mater. 61 (11) (2013) 4237–4244.

[39]Z. Sun, G. Song, J. Ilavsky, G. Ghosh, P.K. Liaw, Nano-sized precipitate stability and its controlling factors in a NiAl-strengthened ferritic alloy, Sci. Rep. 5 (2015) 16081.

[40]P. Pandey, S. Kashyap, D. Palanisamy, A. Sharma, K. Chattopadhyay, On the high temperature

coarsening kinetics of γ precipitates in a high strength Co37. 6Ni35. 4Al9. 9Mo4. 9Cr5. 9Ta2. 8Ti3. 5 fcc-based high entropy alloy, Acta Mater. 177 (2019) 82–95.

[41]S. Neumeier, H. Rehman, J. Neuner, C. Zenk, S. Michel, S. Schuwalow, J. Rogal, R. Drautz, M. Go ken, Diffusion of solutes in fcc cobalt investigated by diffusion couples and first principles kinetic Monte Carlo, Acta Mater. 106 (2016) 304–312.

[42]K.Y. Tsai, M.H. Tsai, J.W. Yeh, Sluggish diffusion in Co-Cr-Fe-Mn-Ni high-entropy alloys, Acta Mater. 61 (13) (2013) 4887–4897.

[43]M. Thompson, C. Su, P.W. Voorhees, The equilibrium shape of a misfitting precipi- tate, Acta Metall. Mater. 42 (6) (1994) 2107–2122.

[44]H. Pottebohm, G. Neite, E. Nembach, Elastic properties (the stiffness constants, the shear modulus and the dislocation line energy and tension) of Ni Al solid solu- tions and of the nimonic alloy PE16, Mater. Sci. Eng. 60 (3) (1983) 189–194.

[45]D. Williams, E. Butler, Grain boundary discontinuous precipitation reactions, Int. Met. Rev. 26 (1) (1981) 153–183.

[46]Y.-J. Chang, A.-C. Yeh, The formation of cellular precipitate and its effect on the tensile properties of a precipitation strengthened high entropy alloy, Mater. Chem. Phys. 210 (2017) 111–119.

[47]J. Nystrom, T. Pollock, W. Murphy, A. Garg, Discontinuous cellular precipitation in a high-refractory nickel-base superalloy, Metall. Mater. Trans. A 28 (12) (1997) 2443–2452.

[48]A. Perovic, G. Purdy, Discontinuous precipitation in Cu-Co alloys, Acta Metall. 29 (1) (1981) 53–64.

[49]K.N. Braszczyńska-Malik, Discontinuous and continuous precipitation in magne- sium aluminium type alloys, J. Alloy. Compd. 477 (1 2) (2009) 870–876.

[50]H.A. Murdoch, C.A. Schuh, Estimation of grain boundary segregation enthalpy and its role in stable nanocrystalline alloy design, J. Mater. Res. 28 (16) (2013) 2154– 2163.

[51]R. Faulkner, Non-equilibrium grain-boundary segregation in austenitic alloys, J. Mater. Sci. 16 (2) (1981) 373–383.

[52]K. Ishida, Effect of grain size on grain boundary segregation, J. Alloy. Compd. 235 (2) (1996) 244– 249.

[53]M. Pouranvari, A. Ekrami, A. Kokabi, Role of base-metal composition in isothermal solidification during diffusion brazing of nickel-based superalloys, Sci. Technol. Weld. Join. 23 (1) (2018) 13–18.

[54]C.-M. Kuo, C.-W. Tsai, Effect of cellular structure on the mechanical property of Al0.2Co1.5CrFeNi1.5Ti0.3 high-entropy alloy, Mater. Chem. Phys. 210 (2018) 103–110.

[55]T.M. Smith, B.D. Esser, N. Antolin, A. Carlsson, R.E. Williams, A. Wessman, T. Hanlon, H.L. Fraser, W. Windl, D.W. McComb, M.J. Mills, Phase transformation strengthening of high-temperature superalloys, Nat. Commun. 7 (2016) 13434.
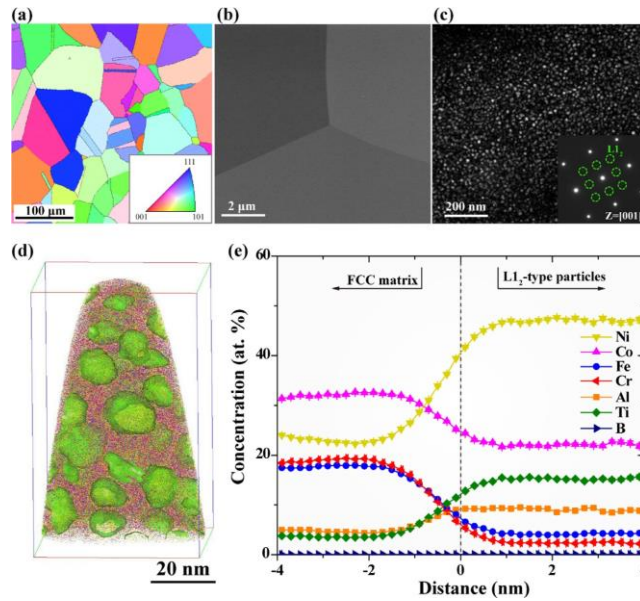
Fig. 1. (a) EBSD mapping of the solid-solution HEA showing a fully recrystallized structure with micron-sized equiaxed grains. (b) Reprehensive SEM image showing the GB morphology with no measurable heterogenous precipitates at the GBs. (c) DF-TEM image and the corresponding SAED pattern (inset) revealing the formation of ordered L1$_2$ nanopar- ticles due to the rapid precipitation kinetics. (d) Atom probe analysis showing tomography of the L1$_2$ nanoparticles. A 10at.% Ti iso-concentration surface is used to highlight the outline of nanoparticles. (e) A proximity histogram constructed across the matrix/particles interface showing the element distributions.
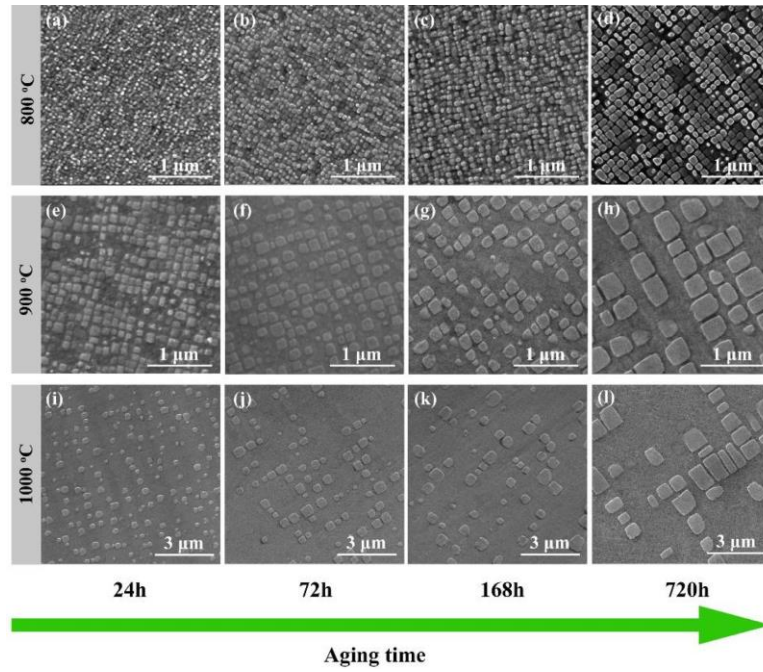
Fig. 2. Representative SEM micrographs showing the temporal evolution of intragranular L12-type nanoparticles in the present Al6Ti6 HEA aged at: (a) 24h, 800°C, (b)72h, 800°C, (c)168h, 800°C, (d)720h, 800°C, (e) 24h, 900°C, (f)72h, 900°C, (g)168h, 900°C, (h)720h, 900°C, (i) 24 h, 1000°C, (j)72h, 1000°C, (k)168h, 1000°C, (l)720 h, 1000°C.
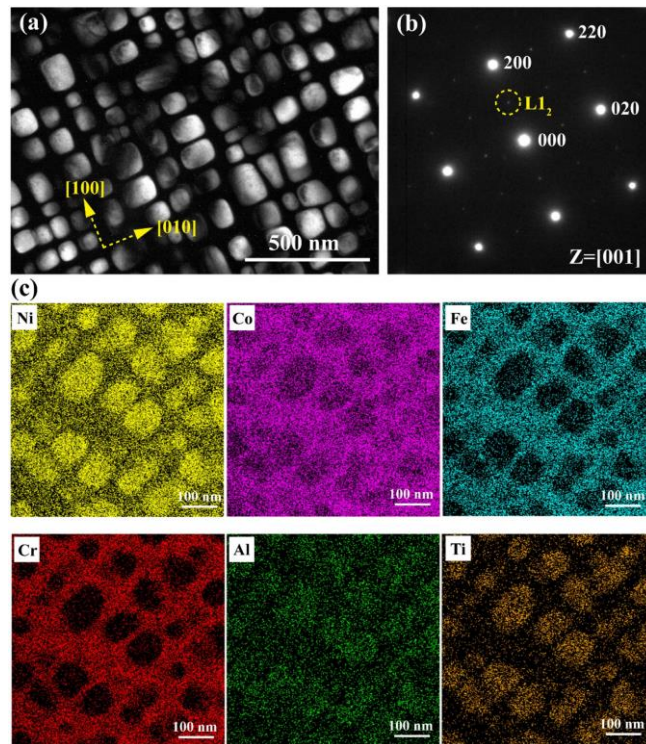
Fig. 3. Representative DF-TEM image (a) and corresponding SADP (b) of the Al6Ti6 HEA aged at 800°C for 720 h. A typical "FCC + $L1_2$" dual-phase structure was clearly confirmed. (c) STEM-EDS map showing the elemental distribution of the $L1_2$-type nanoparticles
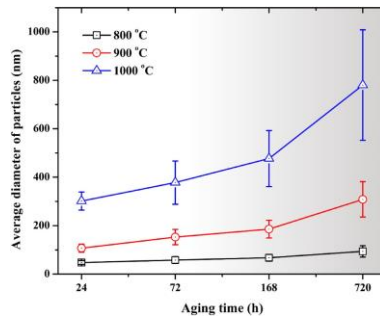
Fig. 4. Plot illustrating the size evolution of the L12-type nanoparticles isothermally aged at 800, 900 and 1000°C for various durations.
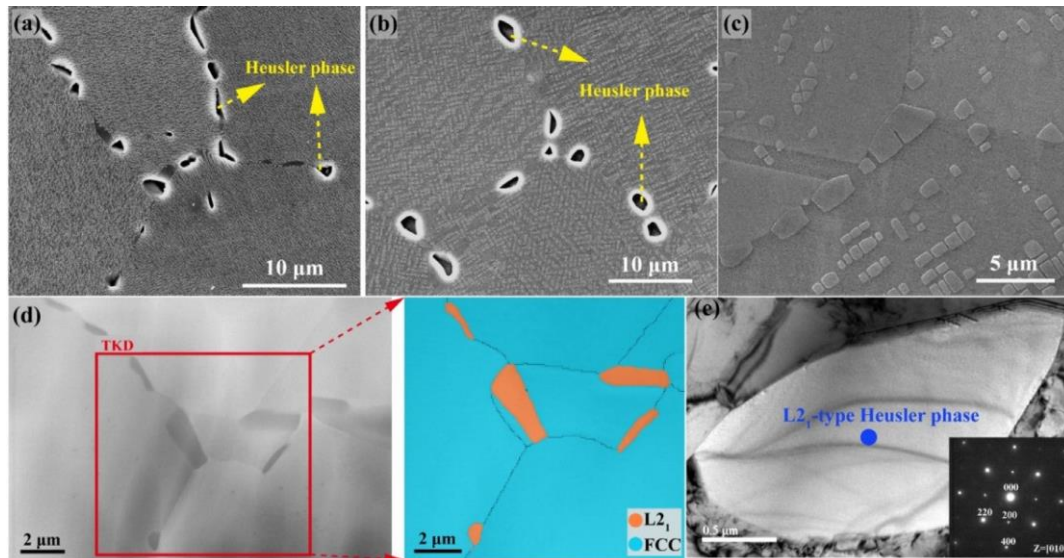
Fig. 5. Representative SEM micrographs showing GB microstructures of the present Al6Ti6 HEA after isothermal aging at (a) 800°C, (b) 900°C, and (c) 1000°C for 720 h. Noticeable microstructural instability can be observed in the samples aged at 800 and 900°C, forming the brittle Heusler phase at grain boundaries. (d) Representative TKD images observed in the HEA aged at 800°C for 720 h showing the distribution of Heusler phase at the GBs. (e) Representative BF-TEM image and corresponding SAED pattern (insert) of the Heusler phase.
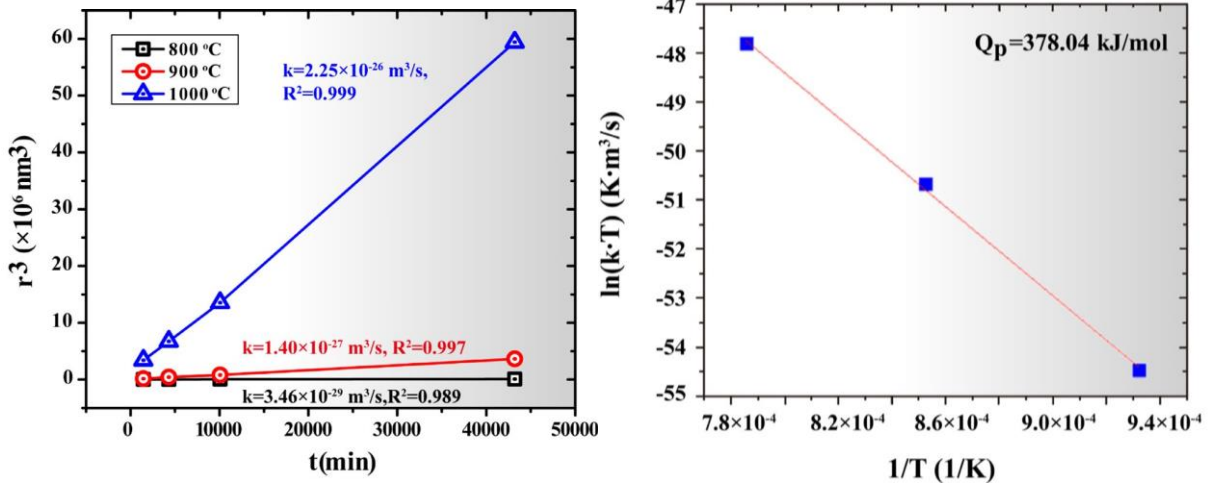
Fig. 6. (a) Plot of the average precipitate size (r^3) versus the aging time (t) for the Al6Ti6 HEA aged

at temperatures between 800°C and 1000°C. (b) Arrhenius plot of the coarsening rate constant

(ln(k¢T)) as a function of the reciprocal aging temperature (1/T) gives the activation energy (Q).

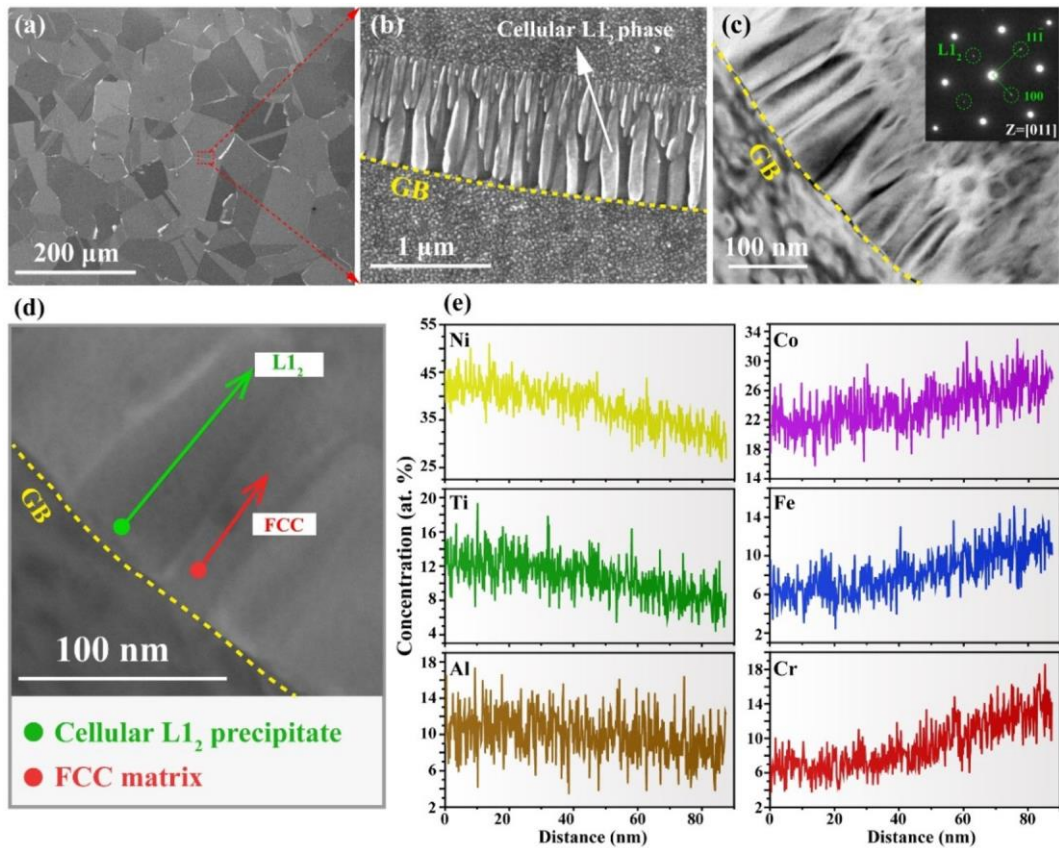**Fig. 7**. (a) Low-magnification SEM image of the Al6Ti6 HEA aged at 800°C for 4 h. (b) High-magnification SEM image of the Al6Ti6 HEA aged at 800°C for 4 h highlighting the formation of discontinuous cellular precipitates at the GBs. (c) Bright-field TEM (BF-TEM) image and corresponding SADP revealing the $L1_2$ structure of these cellular precipitates. (d) & (e) STEM-EDS showing the elemental distributions of the cellular $L1_2$-type precipitates. A pronounced compositional heterogeneity can be clearly observed in the cellular $L1_2$-type pre- cipitates.
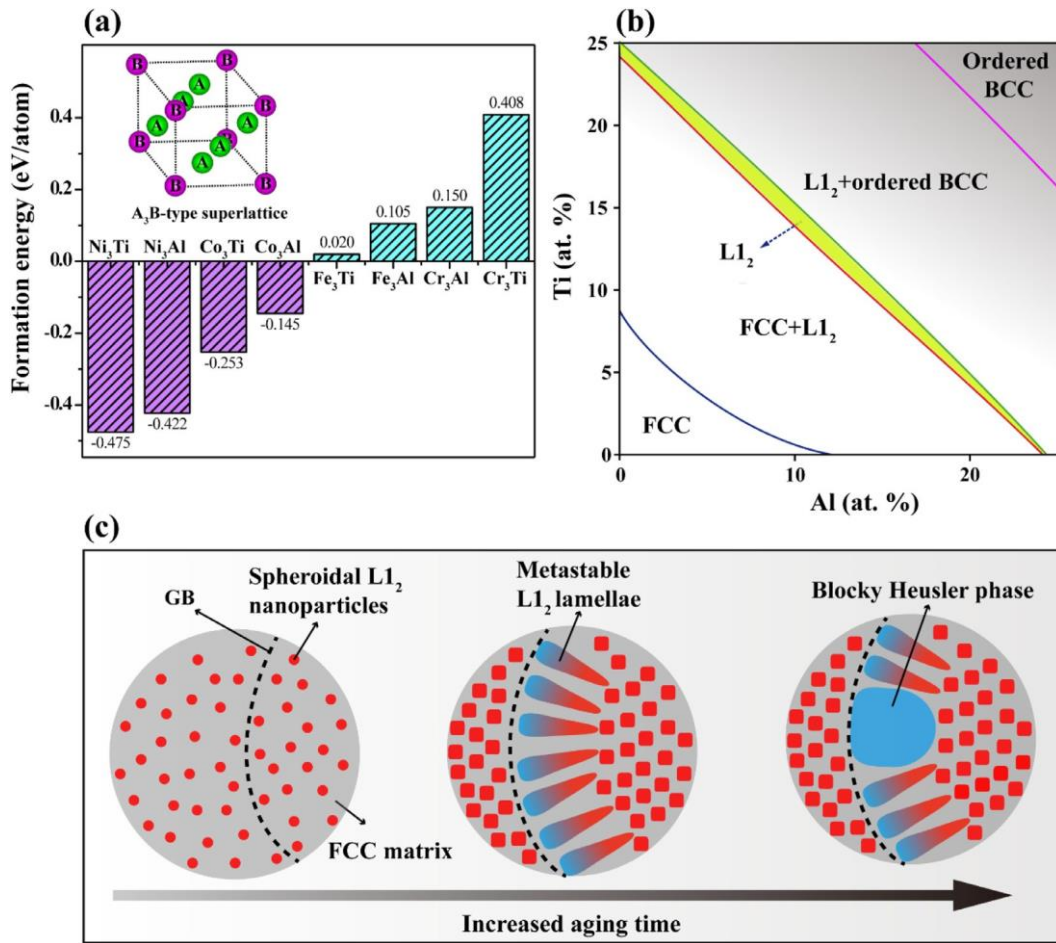
Fig. 8. (a) DFT calculations showing the energetic differences among various L1$_2$-type sub-systems with different atomic pairs. The inset shows the unit cell of L1$_2$ structure with a typical A$_3$B atomic configuration. (b) Thermodynamic calculations showing the effects of Ti and Al additions on the phase stabilities in the Ni-23Co-Ti-Al system aged at 800°C. (c) Schematic illustration showing the complex precipitation pathway from the metastable L1$_2$ to the Heusler phase at the GBs.
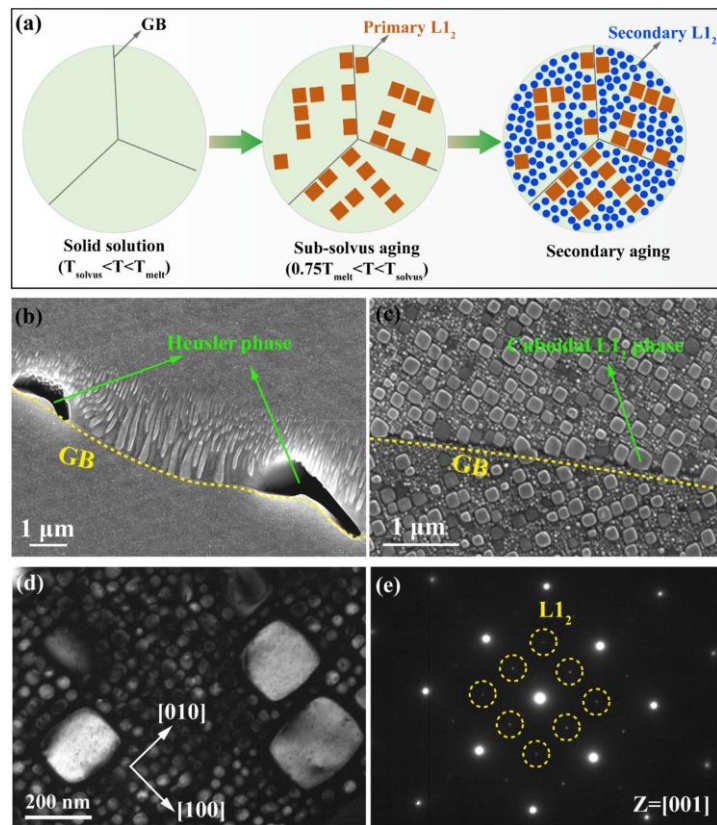
Fig. 9. (a) Schematic illustration of the duplex-aging design for the GB stabilization. (b) SEM image showing the GB structures of the Al6Ti6 alloy aged at 800°C for 24h. (c) SEM image showing the GB structures of the duplex-aged Al6Ti6 alloy, consisting of a sub-solvus aging at 1000°C for 4 h and a secondary aging at 800°C for 24h. (d) DF-TEM image and (e) corresponding SADP revealing the L1$_2$ structure of these precipitates with a bimodal distribution.
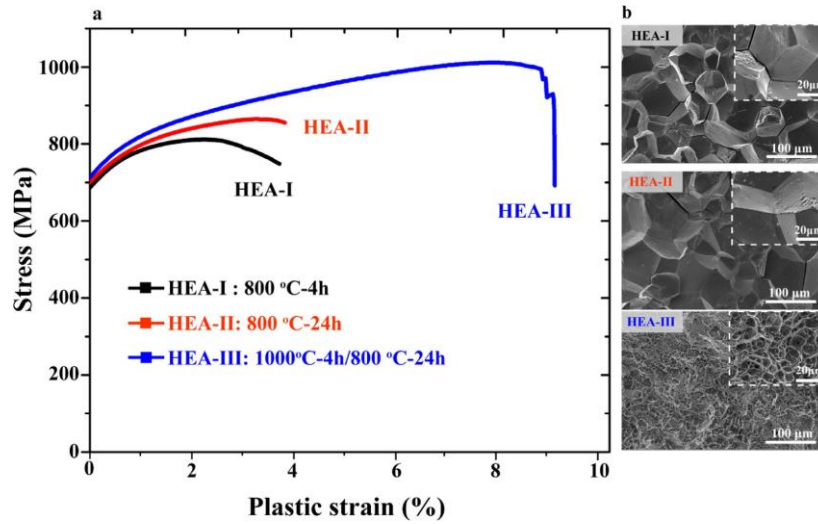
Fig. 10. (a) Uniaxial tensile curves of the investigated HEAs tested at the typical intermediate temperature of 700°C, presenting a distinct brittle-to-ductile transition and a concur- rent increment in tensile strength in the duplex-aged HEA. (b) SEM images showing the fractographic features of the investigated HEAs.